PHYSICAL REVIEW FLUIDS **2**, 053601 (2017)

Orbiting pairs of walking droplets: Dynamics and stability

Anand U. Oza
Courant Institute of Mathematical Sciences, New York University, 251 Mercer Street, New York, New York 10012, USA

Emmanuel Siéfert
Department of Mathematics, Massachusetts Institute of Technology, 77 Massachusetts Avenue, Cambridge, Massachusetts 02139, USA
and Laboratoire PMMH, CNRS, ESPCI, PSL Research University, 10 rue Vauquelin, 75005 Paris, France
and Sorbonne Universités, Université Paris Diderot

Daniel M. Harris
Department of Mathematics, University of North Carolina at Chapel Hill, Phillips Hall CB#3250, Chapel Hill, North Carolina 27599, USA

Jan Moláček
Max Planck Institute for Dynamics and Self-Organization, Am Faßberg 17, 37077 Göttingen, Germany

John W. M. Bush*
Department of Mathematics, Massachusetts Institute of Technology, 77 Massachusetts Avenue, Cambridge, Massachusetts 02139, USA
(Received 6 October 2016; published 9 May 2017)

A decade ago, Couder and Fort [Phys. Rev. Lett. **97**, 154101 (2006)] discovered that a millimetric droplet sustained on the surface of a vibrating fluid bath may self-propel through a resonant interaction with its own wave field. We here present the results of a combined experimental and theoretical investigation of the interactions of such walking droplets. Specifically, we delimit experimentally the different regimes for an orbiting pair of identical walkers and extend the theoretical model of Oza *et al.* [J. Fluid Mech. **737**, 552 (2013)] in order to rationalize our observations. A quantitative comparison between experiment and theory highlights the importance of spatial damping of the wave field. Our results also indicate that walkers adapt their impact phase according to the local wave height, an effect that stabilizes orbiting bound states.

DOI: 10.1103/PhysRevFluids.2.053601

I. INTRODUCTION

A droplet may bounce indefinitely [1] on the surface of a fluid bath subjected to a vertical acceleration $\Gamma = \gamma \cos(2\pi f_0 t)$. Above the bouncing threshold, $\gamma > \gamma_B$, the droplet avoids coalescence by virtue of a thin air layer sustained between the drop and bath during impact. Such droplet levitation has been examined both experimentally [2–5] and theoretically [4,6–8]. Between the so-called walking threshold and Faraday instability threshold, $\gamma_W < \gamma < \gamma_F$, the droplet self-propels by interacting with its own wave field [1,9]. Walking arises because the droplet lands on a perturbed surface, and the local slope imparts a horizontal impulse to the droplet during impact.

*bush@math.mit.edu

The association of a self-propelling drop and extended wave field is referred to as a walker [1]. The transition from bouncing for $\gamma > \gamma_B$ to walking for $\gamma > \gamma_W > \gamma_B$ is preceded by a period-doubling transition [9]; specifically, the drop must bounce at twice the period of the forcing, commensurate with the most unstable mode of the subharmonic Faraday instability [10,11], in order to walk. Faraday waves of wavelength λ_F are thus excited by the resonant interaction between the bath and the drop. The closer the system is to the Faraday instability, the more long-lived the waves. The walker motion is thus influenced by the wave field generated by previous impacts. The concept of path memory [12] is central to the walker dynamics: prediction of the walker's future requires knowledge of its past. The relevant time scale of influence is proportional to the memory parameter, $M_e \propto (1 - \gamma/\gamma_F)^{-1}$, which prescribes the proximity to the Faraday threshold, and so the persistence of the impact-induced wave field.

Walkers are of growing interest because they exhibit numerous phenomena reminiscent of quantum systems: single-particle diffraction [13,14], quantum-like statistical behavior in a corral [15,16], tunneling [17], quantized orbits in a rotating frame [18,19] and central force [20,21], orbital level splitting [22], and spin states [23,24]. This system represents the first macroscopic example of a pilot-wave system of the form envisaged by Louis de Broglie in his double-solution pilot-wave theory [25]. The relation between this hydrodynamic pilot-wave system and the modern extensions of de Broglie's mechanics has been explored elsewhere [23,26].

Couder, Protière and coworkers [1,22,27,28] observed that two walkers may interact through their common wave field, and they reported a variety of behaviors. Depending on the initial conditions, the two droplets either attracted, repelled, or walked side by side in the so-called promenade mode [29]. Circular orbits, oscillatory orbits, or epicycles also arose, depending on the relative size of the two drops. For identical drops, orbital diameters d_n were quantized, such that $d_n = \lambda_F(n - \varepsilon_0)$, where the orbit order $n \in \mathbb{N}^*$ when the two drops were bouncing in phase and $n = 1/2 + k, k \in \mathbb{N}$ when they were out of phase. The quantization was rationalized qualitatively in terms of a simple model for the wave field. The authors reported that ε_0 is typically measured to be 0.2, but depends on different parameters such as the forcing acceleration, drop size, and orbit order n. They also reported the velocity of the orbiting droplets, noting that the orbital motion slows down the drops: the smaller the orbits, the slower the drops. Since the precise values of the forcing acceleration and drop sizes were not reported, a quantitative comparison with theory was not possible. The goal of the experimental portion of our study is to categorize the range of possible orbiting states and their dependence on system parameters. This quantitative data will prove to be essential in guiding the refinement of theoretical models of this hydrodynamic pilot-wave system.

The drop behavior is extremely sensitive to the system parameters, specifically to drop size and forcing acceleration. Moláček and Bush [4,30] described the impact of a bouncing drop on a vibrating liquid bath in terms of a logarithmic spring model. They also calculated the form of the wave field induced by the droplet impacts. This provided the basis for the stroboscopic model of Oza *et al.* [19,31], in which the vertical motion of the droplet is averaged over the bouncing period and the drop is approximated as a continuous moving source of standing waves that decay in time. While easier to analyze than the full model of Moláček and Bush [4,30], the stroboscopic model introduces a parameter in the form of the impact phase, which was chosen to match the walker's rectilinear walking speed. Using a more refined model of weakly viscous quasipotential wave generation and evolution, Milewski *et al.* [32] succeeded in reproducing a number of features observed by Protière *et al.* [28], such as circular orbits and the promenade mode [29]. Moreover, it made clear the importance of spatial damping in accurately modeling the wave field far from a walker. The theoretical models of pilot-wave hydrodynamics are reviewed by Bush [23], and more recent developments include those of Blanchette [6], Dubertrand *et al.* [33], Durey and Milewski [34], and Faria [35]. We here apply and extend the stroboscopic model of Oza *et al.* [19,31] through an investigation of the dependence of the stability of orbiting pairs on both memory and orbital diameter.

II. EXPERIMENTS

A. Apparatus and methods

We use the experimental setup developed by Harris and Bush [36]. The system consists of an electrodynamic shaker with an external linear air bearing that constrains the vibration to a single axis. The maximum inhomogeneity of the vertical vibration amplitude can thus be reduced to approximately 0.1%, and transverse vibrations are effectively eliminated. A piezoelectric droplet-on-demand generator [37], capable of producing droplets of highly repeatable size, is used to create a pair of nearly identical droplets that are released onto the bath surface. In the present study, we restrict our attention to a single drop radius, $R = 0.37 \pm 0.01$ mm, unless otherwise stated, as the walking regime is relatively large for this drop size [Fig. 1(d)]. Orbital bound states can be observed for a range of drop sizes, but are less stable for substantially smaller or larger drops. In order to specify the memory, we need both the driving amplitude and the Faraday threshold, the latter of which depends on the fluid temperature. All experiments were undertaken with a bath of 20 cSt silicone oil of depth $H = 6.5$ mm driven at a vibrational frequency $f_0 = 80$ Hz, for which $\gamma_F \sim 4.2g$ at room temperature.

The experimental apparatus is presented in Fig. 2. In order to eliminate the influence of air currents, a sealed lid is fixed to the vibrating bath. We launch two walkers in opposite parallel directions, the perpendicular distance between their initial trajectories being the impact parameter. These launchers, as used successfully in recent studies [38], allow us to impel the droplet to walk straight along the symmetry axis of the diverging submerged barriers. By laterally translating the launchers, the impact parameter can be varied continuously. To synchronize the two drops, we employ four rotating paddles that pass through a sealed bearing in the lid, as illustrated in Fig. 2. The paddles are partially submerged in the silicone oil and the resulting menisci repel the drops, allowing for drop confinement in the holding pens. The droplet trapping typically takes no more than 30 s, because the droplets tend to follow the curved outer boundary toward the holding pens. Once both droplets are trapped, both front gates are opened simultaneously and the droplets walk through the launchers and interact near the center of the vessel.

This system of paddles and launchers allows us to obtain different orbits by following a simple protocol. First, the impact parameter is set to be close to the diameter of the desired orbit. Then the system is forced just above the bouncing threshold, at typically $1.2g$, and the drops are created.

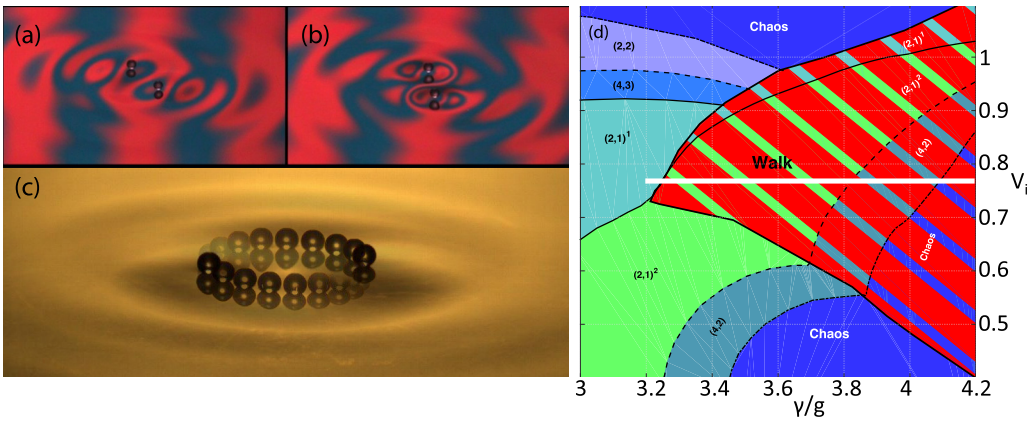

FIG. 1. (a, b) A pair of walkers orbiting in phase in the $n = 1$ orbital mode (Supplemental Movie 1 [39]). (c) Strobed image illustrating the horizontal trajectory of two drops locked in a circular orbit. (d) The parameter regime explored in our experimental study is indicated by the white line. The vibration number $V_i = 2\pi f_0/\sqrt{\sigma/\rho R^3}$ is fixed at 0.77, corresponding to drops of radius $R = 0.37$ mm. The vibrational forcing acceleration of the bath is γ. The relevant variables are defined in Table I.

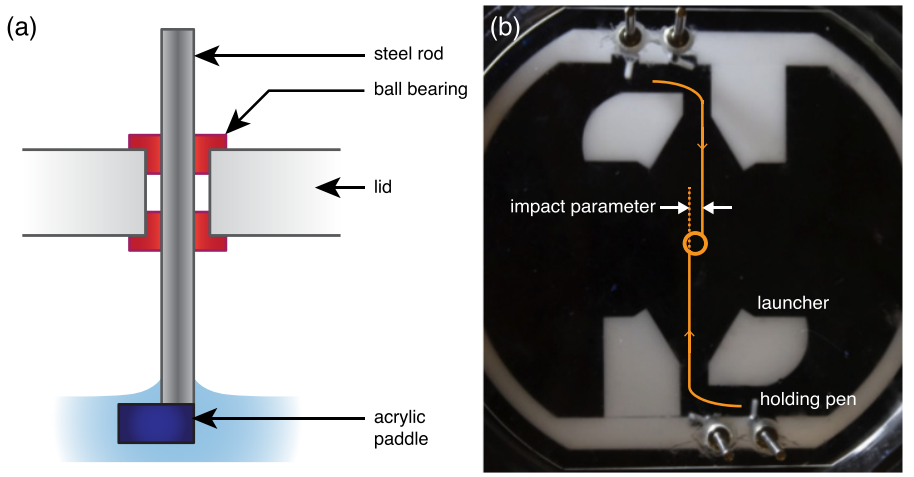

FIG. 2. (a) Schematic illustration of one paddle. (b) Top view of the vessel, with the channels leading to holding pens then two launchers. The orange lines indicate the trajectories of the drops, which exit the launchers before locking into orbital motion in the middle of the vessel.

Next, we increase the vibrational forcing in order to cross the period-doubling transition (typically $\gamma \approx 3g$). A strobe light is used to ascertain whether the two drops are bouncing in or out of phase, and the relative phase may then be altered by perturbing the fluid surface near one of the drops with a partially immersed needle. We then replace the lid and increase the forcing to the desired value $\gamma > \gamma_W$ and use the paddle mechanism to launch the two drops simultaneously. Provided the orbit is relatively well centered in the vessel, so that the influence of boundaries is minimized, we vary the forcing acceleration γ incrementally, waiting approximately one minute until the system reaches a new steady state. We then acquire the trajectories (for typically 30 s) using a top-view camera. Each video (shot at 20 frames per second) is then postprocessed and analyzed to obtain the position of the two drops at every time step using tracking software, yielding walker trajectories.

B. Experimental results

To characterize the quantized orbits, we follow the notation of Protière *et al.* [27], using integer orbit orders n to denote orbits when the two drops are in phase, and half-integers when they are out of phase. We observed seven different orbit sizes, from $n = 0.5$ to 3.5. While larger orbits may be possible, we were constrained experimentally by the finite size of our vessel and the influence of boundaries. The orbit orders $n = 3$ and $n = 3.5$ have not previously been reported [22,27,28] but were achieved here presumably by virtue of the precision of the driving system and the elimination of air currents. Evidently, for such large orbits, the attractive wave force exerted by the other drop may be exceeded by the influence of air currents. A video of an $n = 1$ orbit is shown in Supplemental Movie 1 [39] and still images in Fig. 1. Figure 3 shows six different orbital trajectories achieved at approximately the same forcing. It highlights the fact that the orbital diameters are quantized, and span a sizable range, from 1.1 mm $\sim 3R$ between the centers of the two drops for $n = 0.5$ to approximately 16 mm $\sim 40R$ for $n = 3.5$. For small orbit orders n, the drop velocity is substantially less than the associated free walking speed u_0 of a single walker, an effect that will be rationalized in Sec. III.

The dependence of orbital stability on memory is reported in Fig. 4. We consider all of the orbits that could be achieved with our fixed drop size and observe several dynamical regimes. For $n = 0.5$, we observe that the pair of drops does not walk in a considerable range above the walking threshold for single drops (gray region). This delayed onset of walking might be explained by the fact that the two wave fields generated by the out-of-phase pair of drops are so close that they roughly cancel each other, resulting in a wave field that is locally almost flat. At low memory, small orbits ($n \leqslant 2$)

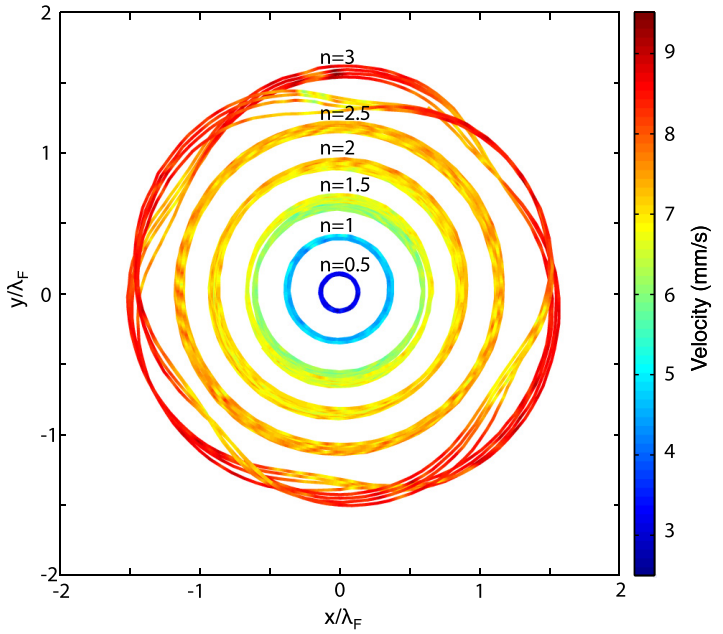

FIG. 3. Observed trajectories of orbiting pairs of walkers, from the innermost orbit order $n = 0.5$ to the outermost $n = 3$ at forcing acceleration $\gamma/\gamma_F = 0.86 \pm 0.01$. The radius of all drops is $R = 0.37 \pm 0.01$ mm and the Faraday wavelength $\lambda_F = 4.75$ mm. Color bar indicates the instantaneous speed in mm/s. The free walking speed of a single walker at this value of γ/γ_F is $u_0 = 7.9 \pm 0.3$ mm/s. The $n = 3.5$ orbit is a wobbling trajectory at this value of memory (see Fig. 4).

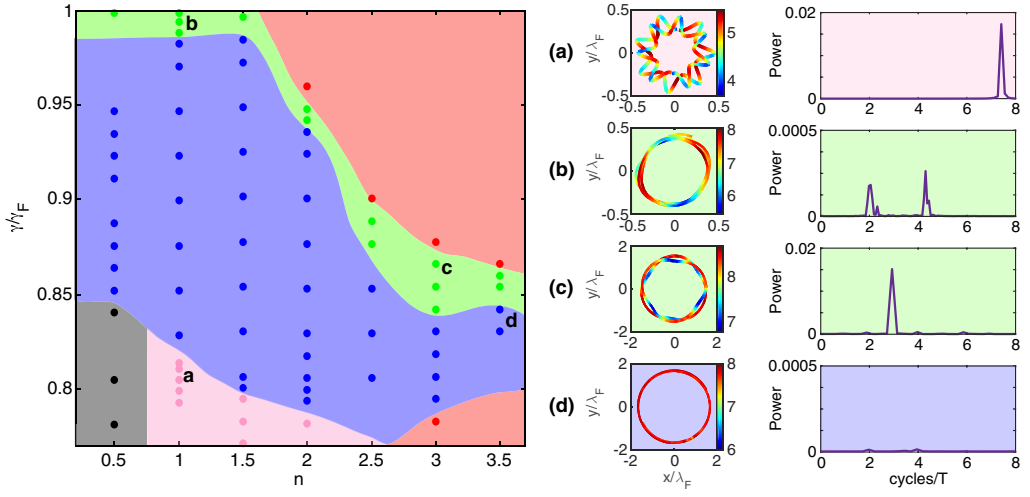

FIG. 4. Orbital stability diagram for pairs of walkers of the same size, $R = 0.37 \pm 0.01$ mm, forced above the walking threshold, $\gamma/\gamma_F \geqslant \gamma_W/\gamma_F = 0.77 \pm 0.01$. Each dot corresponds to one orbital trajectory acquired over 30 s, and n is the orbit order. Blue dots correspond to stable circular trajectories, rose dots to wobbling at low forcing acceleration, green dots to wobbling at large forcing acceleration, red dots to unstable orbits, and black dots to stationary bouncing. Four typical trajectories are shown in panels (a)–(d), along with power spectra of the interdroplet distance, T being the orbital period. The color bars indicate the droplet speed in mm/s. The trajectories correspond to (a) high-frequency wobbling at low memory, (b) 2ω-wobbling at high memory, (c) 3ω-wobbling at high memory, and (d) stable circular motion.

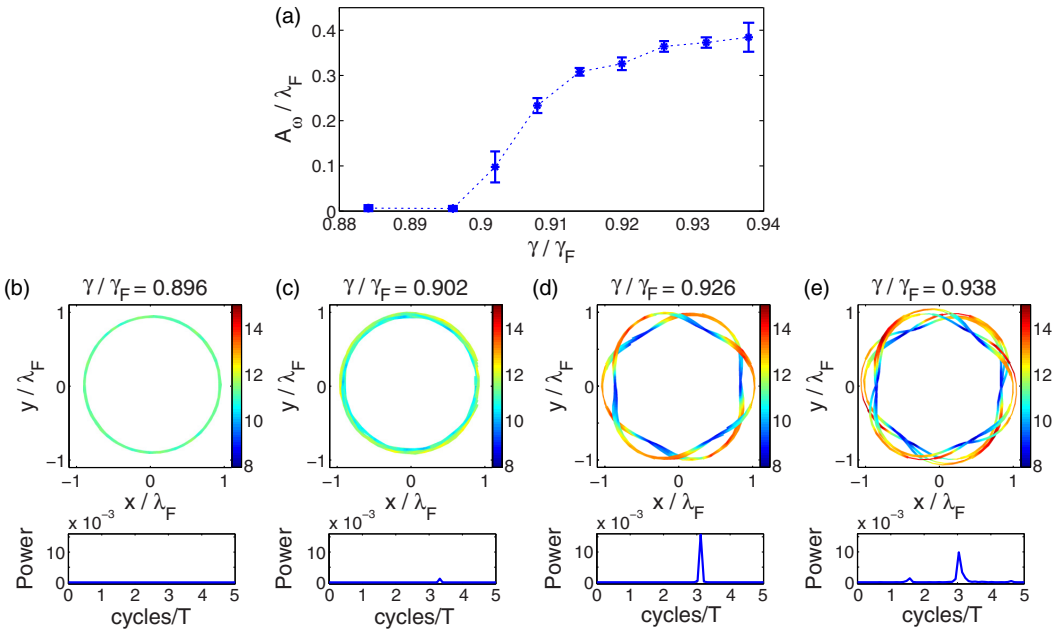

FIG. 5. Evolution of the wobbling amplitude as a function of memory for two drops of radius $R = 0.4 \pm 0.01$ mm orbiting in the $n = 2$ mode. (a) Dependence of the wobbling amplitude A_w on forcing acceleration γ/γ_F. The amplitude is measured as the mean of the successive peak-to-peak distances between the walkers, and error bars reflect the standard deviation of the measurement. (b)–(e) Four orbital trajectories at specified memories, the color indicating the speed in mm/s. Also shown are power spectra of the distance between the two drops, T being the orbital period. One can see the appearance of several modes of oscillation at high memory (e).

exhibit a distinct transition from a bouncing state to a wobbling orbit, characterized by a periodic oscillation in the separation distance between the walkers. This low-memory wobbling region gets smaller with increasing n. The small orbits ($n \leqslant 1.5$) remain bound at high memory, even just below the Faraday threshold. In the central (blue) region, we observe circular orbits of the form described by Protière *et al.* [28]. At higher values of memory (red region), large circular orbits ($n \geqslant 2$) are unstable, but stable wobbling orbits (green region) typically arise prior to the onset of instability.

The wobbling styles arising at low and high memory are denoted by different colors in Fig. 4 because they appear to have different origins. Typical trajectories of the different wobbling styles are shown in Fig. 4. At low memory, wobbling appears to be associated with the transition from the static bouncing state to circular motion. Particularly for $n = 1$, at the walking threshold for single drops, the drops begin to oscillate along a line. When the forcing acceleration is increased, this oscillating pair begins to slowly rotate around its center of mass [Fig. 4(a)]. As the memory is progressively increased, the wobbling decreases in amplitude and ultimately disappears. At high memory, both 2ω- and 3ω-wobbling orbits are observed [Figs. 4(b) and 4(c)]: the separation distance between the drops oscillates at roughly twice or thrice the orbital frequency, which is apparent from the peaks in the power spectra of the interdroplet distance. These wobbling orbits are thus locked on the orbital period, in contrast to those observed at low memory. The growth of the wobbling amplitude with increasing memory is reported in Fig. 5(a), behavior suggestive of a Hopf-type instability. The wobbling trajectories in Figs. 5(d) and 5(e) exhibit substantial speed fluctuations, as the walkers accelerate when they move apart and decelerate when they come together.

In Fig. 6 we report the dependence of the mean speed of orbiting walkers on the forcing acceleration γ/γ_F. Error bars represent the standard deviation of the speeds; thus, large error

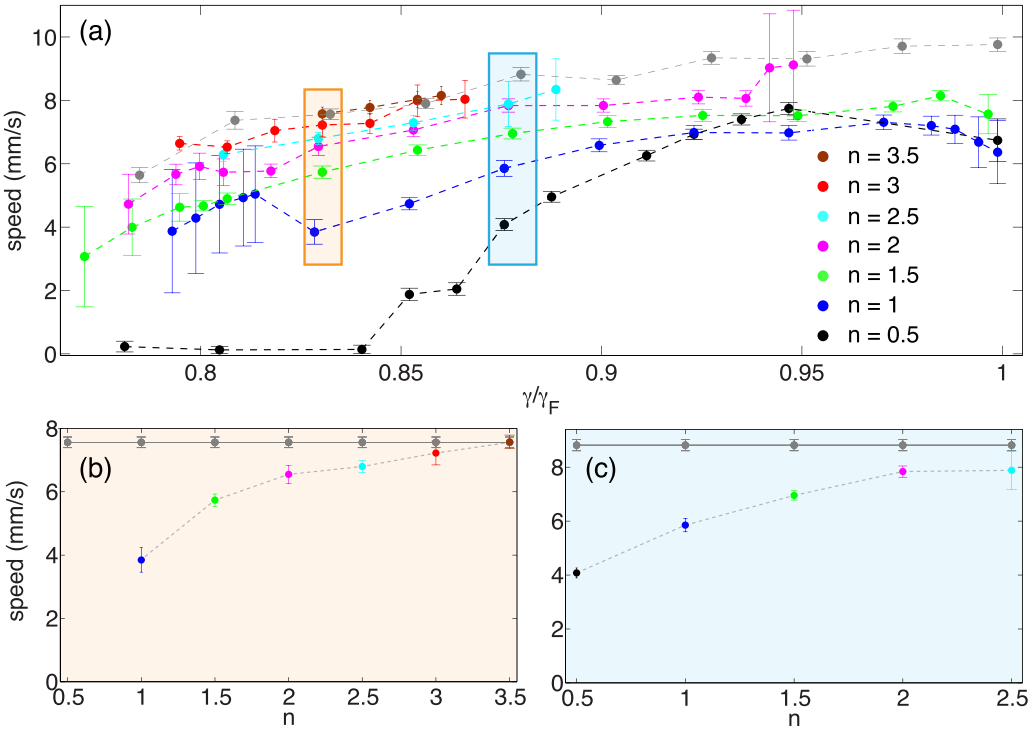

FIG. 6. (a) The observed dependence of the mean velocity of the orbiting drops on the forcing acceleration γ/γ_F, colors indicating the orbit order n. Error bars are due to velocity fluctuations associated with orbital oscillations, slight differences in drop size, and measurement error. The two walkers maintain orbital speeds within ∼17% of each other, and typically within ∼9%. The gray data correspond to the rectilinear walking speed of a single free walker. Panels (b) and (c) show the velocity of the orbiting drops as a function of the orbit order n at a fixed memory, specifically (b) $\gamma/\gamma_F = 0.83 \pm 0.0025$ and (c) $\gamma/\gamma_F = 0.8775 \pm 0.0025$.

bars are indicative of wobbling orbits. A clear tendency is observed: walker speeds increase with memory and then plateau for $\gamma/\gamma_F > 0.9$. Orbital speed appears to decrease slightly in the high memory limit, $\gamma/\gamma_F > 0.975$. At fixed memory, walkers in orbiting pairs are generally slower than free walkers, although the maximum speed in a wobbling orbit may exceed the free walking speed. Figures 6(b)–6(c) show that the speed increases monotonically with n, a trend also reported by Protière *et al.* [28]. A similar trend was observed for promenading pairs of droplets by Borghesi *et al.* [29], who interpreted this as evidence of an effective binding energy between walkers.

III. THEORETICAL MODELING AND COMPARISON WITH EXPERIMENT

A. Theoretical model

We here outline an improved version of the stroboscopic model introduced by Oza *et al.* [19,31], developed with a view to rationalizing the experimental results described in Sec. II. We consider two walkers of mass m, radius R, density ρ, and surface tension σ with horizontal positions $\boldsymbol{x}_1(t)$ and $\boldsymbol{x}_2(t)$ bouncing in phase ($\varsigma = +1$) or out of phase ($\varsigma = -1$) under a gravitational acceleration g, the relevant variables being given in Table I. Walkers experience two forces in the horizontal direction [9,30]: a propulsive wave force proportional to the local slope of the fluid surface and an opposing drag force proportional to their velocity. A force balance in the horizontal direction, time-averaged over the bouncing period T_F, yields the pair of trajectory equations [30]

$$m\ddot{\boldsymbol{x}}_i + D\dot{\boldsymbol{x}}_i = -mg\mathcal{S}(h_i(\boldsymbol{x}_i,t))\nabla h_i(\boldsymbol{x}_i,t) \tag{1}$$

TABLE I. Variables and parameters appearing in the trajectory equation (1)–(2). Following the experiments described in Sec. II, we model walkers of radius $R = 0.37$ mm and viscosity $\nu = 20$ cSt forced at a frequency $f_0 = 80$ Hz. The numerical values of the corresponding constants appearing in the trajectory equations are [30] $T_F = 0.025$ s, $T_d = 0.0182$ s, $k_F = 1.32$ mm^{-1}, $\lambda_F = 4.75$ mm, $m = 2.01 \times 10^{-4}$ g, $D = 1.55 \times 10^{-3}$ g/s, $A = 13.8\,\mu$m, $\alpha = 4.31 \times 10^{-4}$ s/mm^2.

Variables	Definition
$\boldsymbol{x}_1(t), \boldsymbol{x}_2(t)$	Drop positions
m, R	Drop mass, radius
g, γ, f_0	Gravitational acceleration, forcing acceleration, forcing frequency
γ_F, k_F, λ_F	Faraday instability threshold, wave number, wavelength
T_d, $T_F = 2/f_0$	Decay time of waves without forcing, Faraday period
σ, ρ, H	Fluid surface tension, density, mean depth
(ν_e) ν	(Effective [30]) fluid kinematic viscosity
μ_a, ρ_a	Air dynamic viscosity and density
$\mathcal{S} = \sin\Phi$	Sine of wave's mean phase during contact time
$\varsigma = \pm 1$	Drops' relative bouncing phase
$D = 0.17mg\sqrt{\frac{\rho R}{\sigma}} + 6\pi\mu_a R(1 + \frac{\rho_a g R}{12\mu_a f_0})$	Drag coefficient
$A = \frac{\sqrt{8\pi\nu_e T_F}}{3}\frac{(k_F R)^3}{3\mathrm{B_w}^{-1}+1}$, $\mathrm{B_w} = \frac{\rho g}{k_F^2\sigma}$	Wave amplitude, Bond number
$\alpha = \frac{\epsilon^2}{2\nu_e(1+2\epsilon^2)}$ where $\epsilon = \frac{2\pi f_0 k_F \nu_e}{g(3\mathrm{B_w}^{-1}+1)}$	Wave spatial damping coefficient
$M_e = \frac{T_d}{T_F(1-\gamma/\gamma_F)}$	Memory parameter

for $i = 1,2$, where D is the time-averaged drag coefficient, h_i the wave field generated by the two walkers, and $\mathcal{S} = \sin\Phi$ is the sine of the mean phase of the wave relative to the forcing during the drop's contact with the bath. Note that $\mathcal{S}$ depends on both the forcing acceleration γ/γ_F and the local wave height h. Including this dependence represents a significant extension to the stroboscopic model, since prior work [19,20] assumed $\mathcal{S}$ to be constant, an approximation we demonstrate to be inadequate in Sec. III B.

The qualitative dependence of the phase parameter $\mathcal{S}$ on the forcing acceleration γ/γ_F and local wave height h may be deduced from the following physical argument. Under the assumption of short contact time, the impact phase must decrease as the bath's peak vertical velocity increases, so as to keep the drop's outgoing vertical velocity roughly constant and thus maintain a periodic bouncing dynamics. The bath's peak vertical velocity increases with forcing acceleration but decreases with local wave height, since a walker in a $(2,1)^2$ bouncing state strikes the bath while the wave is decreasing in amplitude [30]. We thus expect $\mathcal{S}$ to decrease with forcing acceleration and increase with local wave height.

A derivation of the wave field $h_i(\boldsymbol{x},t)$ is given elsewhere [40], an abbreviated version of which is presented here. The linear theory [10,11] of Faraday waves below the Faraday instability threshold, $\gamma/\gamma_F \lesssim 1$, shows that the least stable mode has wave number k_F and frequency $f_0/2$, where the Faraday wave number k_F approximately satisfies the standard water-wave dispersion relation, $(\pi f_0)^2 = (gk_F + \sigma k_F^3/\rho)\tanh(k_F H)$. The mode decays exponentially in time due to viscosity, over a time scale prescribed by the nondimensional memory parameter [12,30], M_e (see Table I). Note that a period-doubled walker is resonant with this mode. Since the wave generated by each impact is small in amplitude, the complete wave field may be obtained by summing the contributions of each walker over its trajectory [4,12,41].

Since the present study concerns interactions between drops separated by several Faraday wavelengths, the model of the emitted standing waves must be reasonably accurate in the far field, which was evidently not required to capture the dynamics of a single walker [19,31]. The wave field generated by a single impact may be approximated by a standing wave with wave number k_F whose amplitude decays exponentially in time, multiplied by a Gaussian profile of time-dependent width [40,42]:

$$h_1(\boldsymbol{x},t) = \frac{A}{T_F}\int_{-\infty}^{t} [f(|\boldsymbol{x}-\boldsymbol{x}_1(s)|,t-s) + \varsigma f(|\boldsymbol{x}-\boldsymbol{x}_2(s)|,t-s)]\,ds, \quad \text{where}$$
$$f(r,t) = J_0(k_F r)\mathrm{e}^{-\alpha r^2/(t+T_F)}\mathrm{e}^{-t/(T_F M_e)}, \tag{2}$$

where α is the spatial damping coefficient, A the amplitude of a single surface wave, and J_0 the Bessel function of the first kind. The corresponding formula for h_2 is obtained by interchanging $1 \leftrightarrow 2$ in Eq. (2). The discrete sum of waves may be replaced by an integral provided the timescale of horizontal motion is long relative to that of the vertical motion [31], $\lambda_F/|\dot{\boldsymbol{x}}_i| \gg T_F$, as is the case in the experiments. The spatial damping factor may be derived [40] as a long-time asymptotic approximation of the wave field generated by a single droplet impact, and arises from the observation that waves of wave number $k \neq k_F$ are damped far more strongly than those with $k = k_F$. The T_F term in the spatial damping factor ensures that $f(r,t)$ and its spatial derivatives are well behaved for all $t \geqslant 0$. We omit the $t^{-1/2}$ term in the interest of simplicity, as it is subdominant to the exponential temporal decay. The model (2) is consistent with experimental measurements of the wave field generated by a single bouncing droplet below the walking threshold [42].

We introduce the dimensionless variables $\hat{\boldsymbol{x}} = k_F\boldsymbol{x}$ and $\hat{t} = t/T_F M_e$, and obtain the dimensionless trajectory equation

$$\kappa\hat{\boldsymbol{x}}_i'' + \hat{\boldsymbol{x}}_i' = -\beta\mathcal{S}(\hat{h}_i(\hat{\boldsymbol{x}}_i,\hat{t}))\nabla\hat{h}_i(\hat{\boldsymbol{x}}_i,\hat{t}),$$
$$\hat{h}_1(\hat{\boldsymbol{x}},\hat{t}) = \int_{-\infty}^{\hat{t}} [\hat{f}(|\hat{\boldsymbol{x}}-\hat{\boldsymbol{x}}_1(\hat{s})|,\hat{t}-\hat{s}) + \varsigma\hat{f}(|\hat{\boldsymbol{x}}-\hat{\boldsymbol{x}}_2(\hat{s})|,\hat{t}-\hat{s})]\,d\hat{s}, \tag{3}$$

where primes denote differentiation with respect to $\hat{t}$, $\hat{f}(\hat{r},\hat{t}) = M_e J_0(\hat{r})\exp(-\frac{\hat{\alpha}\hat{r}^2}{\hat{t}+M_e^{-1}} - \hat{t})$, $\kappa = m/DT_F M_e$, $\beta = mgAk_F^2 T_F M_e/D$, and $\hat{\alpha} = \alpha/(k_F^2 T_F M_e)$. We note that this definition of β differs from that used in prior work [31] and drop all carets in the remainder of the section for the sake of clarity.

B. Phase adaptation of walking droplets

We now use the experimental data presented in Sec. II to empirically deduce the dependence of the phase parameter $\mathcal{S} = \sin\Phi$ on the forcing acceleration γ/γ_F and wave height h. We seek orbital solutions to the trajectory equation (3) of the form $\boldsymbol{x}_1(t) = r_0(\cos\omega t, \sin\omega t)$ and $\boldsymbol{x}_2(t) = -r_0(\cos\omega t, \sin\omega t)$, in which the walkers traverse a circle of radius r_0 at uniform angular velocity ω while diametrically opposed to each other. In doing so, we obtain a system of algebraic equations that describe the radial and tangential force balance on an orbiting pair, thus defining the orbital radius r_0 and angular frequency ω in terms of the experimental parameters:

$$-\kappa r_0\omega^2 = \beta\mathcal{S}\int_0^\infty \left[S_1(z)\sin\frac{\omega z}{2} + \varsigma C_1(z)\cos\frac{\omega z}{2}\right]dz,$$
$$r_0\omega = \beta\mathcal{S}\int_0^\infty \left[S_1(z)\cos\frac{\omega z}{2} - \varsigma C_1(z)\sin\frac{\omega z}{2}\right]dz, \tag{4}$$

where we define the functions

$$S_k(z) = -\frac{\partial^k f}{\partial r^k}\left(2r_0\sin\frac{\omega z}{2}, z\right) \quad \text{and} \quad C_k(z) = -\frac{\partial^k f}{\partial r^k}\left(2r_0\cos\frac{\omega z}{2}, z\right). \tag{5}$$

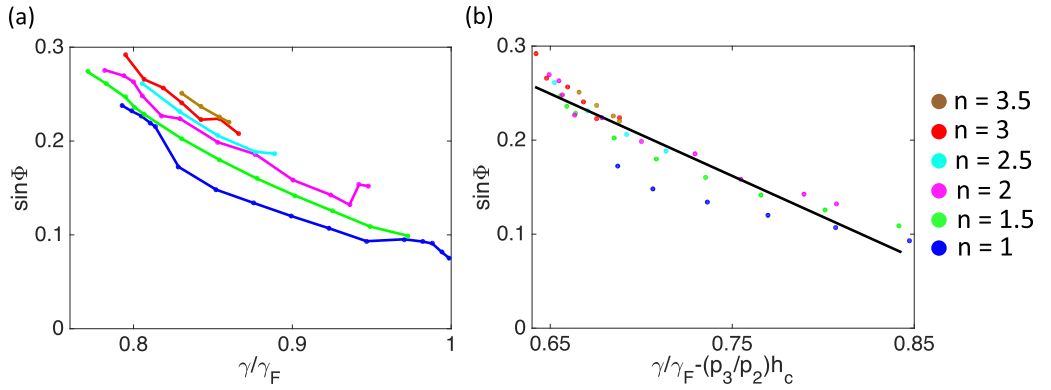

FIG. 7. (a) Dependence of the phase parameter $\sin\Phi$ on the forcing acceleration γ/γ_F and orbit order n, as deduced from the experimental data. The phase is chosen to match the experimentally observed orbital speed using the stroboscopic model described in the text. (b) Empirical fit $\sin\Phi = p_1 - p_2[\gamma/\gamma_F - (p_3/p_2)h_c]$ to the experimental data, where h_c is the local wave amplitude defined in Eq. (6), $p_1 = 0.8171$, $p_2 = 0.8735$, and $p_3 = 5.063 \times 10^{-2}$. We select data points for which $\gamma/\gamma_F \leqslant 0.95$ and the orbital diameter's standard deviation is less than $0.1\lambda_F$, so as to exclude complex bouncing states and wobbling orbits.

We solve Eq. (4) in Matlab, finding the phase parameter $\mathcal{S} = \sin\Phi$ required to match the experimentally observed orbital speed $r_0\omega$ for each value of forcing acceleration γ/γ_F and orbit order n. As shown in Fig. 7(a), this fitted phase parameter generally decreases with forcing acceleration and increases with orbit order n. Both trends are in agreement with the physical argument presented in Sec. III A: since a walker in a circular orbit lies near the trough of the wave created by its orbiting pair, the total wave height at each walker's location is reduced by the presence of the other. These troughs decrease in amplitude with increasing orbit order n, so the total wave amplitude felt by a walker increases with orbital diameter. Since the phase parameter $\mathcal{S}$ is expected to decrease with increasing wave height h, it should increase with increasing orbital diameter.

We proceed by defining the wave height at a walker's position when it is in circular orbit:

$$h_c = -\int_0^\infty [S_0(z) + \varsigma C_0(z)]\, dz. \tag{6}$$

Guided by recent developments reported elsewhere [40], we assume for the sake of simplicity that $\mathcal{S}$ is a linear function of both forcing acceleration γ/γ_F and local wave height h_c. We compute h_c using the experimentally observed orbital radius r_0 and angular frequency ω, restricting our attention to stable circular orbits satisfying $\gamma/\gamma_F \leqslant 0.95$ and thus neglecting walkers in complex bouncing states [Fig. 1(d)]. Multivariate linear regression in Matlab is used to find the line of best fit, $\mathcal{S} = p_1 - p_2(\gamma/\gamma_F) + p_3 h_c$, as shown in Fig. 7(b). In Sec. III C, we shall use this semiempirical linear relationship to assess the existence and stability of orbital solutions to the stroboscopic model (3). This analysis will suggest that the walker behaves as a phase-adapting oscillator, changing its impact phase based on the local wave field so as to maintain a periodic vertical bouncing dynamics.

C. Orbital solutions and their stability

Solving the system of algebraic equations (4)–(6) in Matlab, we find that the orbital solutions are quantized in radius, and that the predicted radii are in good agreement with experiment, as is evident from the solid lines in Fig. 8(c). The spatial damping factor $e^{-\alpha r^2/(t+T_F)}$ is essential to obtain accurate predictions; indeed, Fig. 8(a) shows that the predicted orbits are too small if spatial damping is neglected ($\alpha = 0$), presumably because the model then overpredicts the wave amplitude in the far field [40].

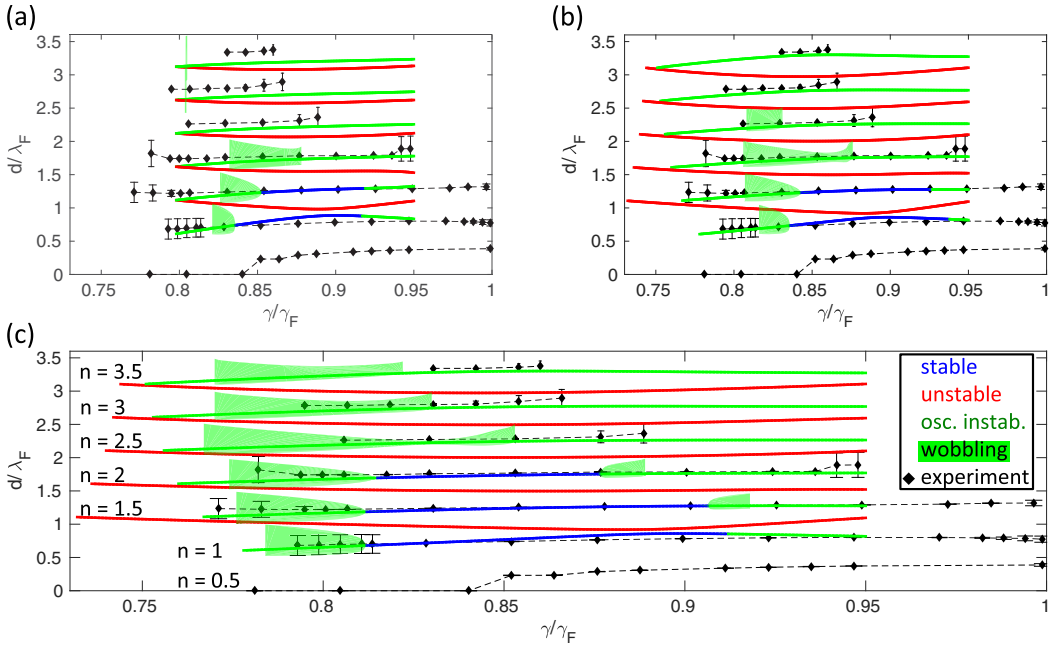

FIG. 8. The dependence on memory of the mean distance d between the orbiting drops for different orbit orders n. (a) The results of a model in which spatial damping is neglected ($\alpha = 0$), and the phase is assumed to be constant ($\sin\Phi = 0.2$). (b) The results of the model in which spatial damping is included, and the phase is assumed to be a different constant for each circular orbit, $\sin\Phi = \mathcal{S}(h_c)$, where h_c is the wave height defined in Eq. (6). (c) The results of the full model in which spatial damping and phase adaptation are included, so that the phase is allowed to change with time, $\mathcal{S} = p_1 - p_2(\gamma/\gamma_F) + p_3 h$. Diamonds correspond to the experimental results. The mean of the successive maxima and minima are plotted for wobbling orbits (green), the standard deviations being on the order of the pixel size. The curves correspond to the theoretical predictions of (4), colored according to the results of our stability analysis. Blue indicates stable orbits, and (red) green indicates orbits that destabilize via a (non) oscillatory instability. The shaded green surfaces indicate the extent of the wobbling orbits found by numerical simulation of the trajectory equation (3). Integer (half-integer) values of n correspond to $\varsigma = 1$ ($\varsigma = -1$). The sign of ς also alternates across different red branches, with the lowest red branch corresponding to $\varsigma = 1$.

Figure 9 shows the dependence of the predicted orbital speed $r_0\omega$ on forcing acceleration γ/γ_F and orbit order n. The results deduced from a model that neglects both spatial damping ($\alpha = 0$) and phase adaptation ($\sin\Phi = 0.2$) are shown in Fig. 9(a), while those corresponding to the full model with both spatial damping and phase adaptation $\sin\Phi = \mathcal{S}(h)$ are shown in Fig. 9(b). The free walking speed u_0 of an isolated walker satisfies the equation

$$u_0 = -\beta\mathcal{S}(h_w)\int_0^\infty \frac{\partial f}{\partial r}(u_0 z, z)\,dz, \quad \text{where} \quad h_w = \int_0^\infty f(u_0 z, z)\,dz. \tag{7}$$

It is evident from Fig. 9(b) that orbiting walkers move slower than they would in isolation, and that their speed increases with orbit order n, as observed in experiment (Fig. 6). We note that the substantial increase of orbital speed with n [Fig. 9(b) inset] is due to the phase parameter $\mathcal{S}$ increasing with local wave height h, an effect that is absent if phase adaptation is neglected [Fig. 9(a)]. Indeed, neglecting phase adaptation leads to circular orbits whose speed changes little with n and may even slightly *decrease* with n. We thus conclude that walkers in orbiting pairs are slower than free walkers owing largely to their phase adaptation based on the local wave field.

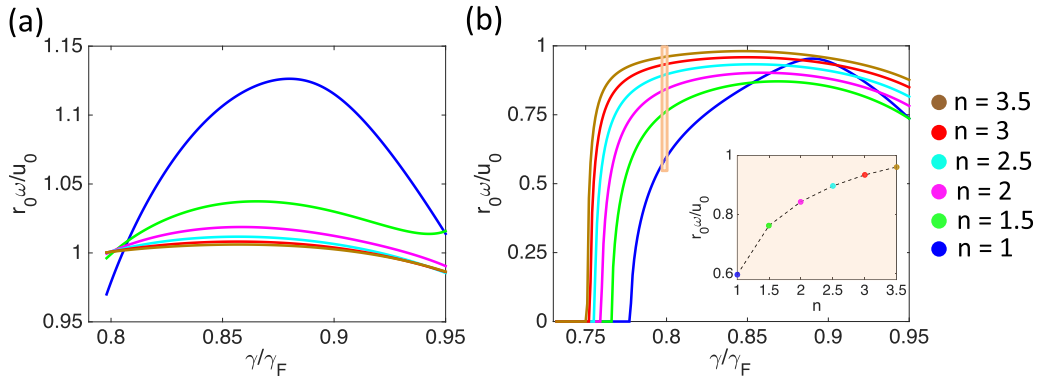

FIG. 9. The dependence of orbital speed $r_0\omega$ on forcing acceleration γ/γ_F and orbit order n, as predicted by (4). The rectilinear walking speed of an isolated walker is denoted by u_0. (a) The results of a model that neglects both spatial damping ($\alpha = 0$) and phase adaptation ($\sin\Phi = 0.2$ is fixed); (b) the results of the full model that incorporates both. The inset in panel (b) shows the dependence of $r_0\omega/u_0$ on n for $\gamma/\gamma_F = 0.8$. As in experiment (Fig. 6), orbiting walkers move slower than they would in isolation, and their speed increases with orbit order n.

We then perform a stability analysis of the orbital solutions by generalizing the framework of Oza *et al.* [19] and Labousse *et al.* [20] to incorporate multiple walkers, the effect of spatial damping, and the dependence of the phase parameter $\mathcal{S}$ on the local wave height. We express the trajectory equations (3) using polar coordinates, $\boldsymbol{x}_1(t) = r_1(t)(\cos\theta_1(t), \sin\theta_1(t))$ and $\boldsymbol{x}_2(t) = r_2(t)(\cos\theta_2(t), \sin\theta_2(t))$, as shown in Eq. (A1) of the Appendix. Following the procedure described in Oza *et al.* [19], we linearize the trajectory equation around the orbiting solution to assess its stability, and so substitute the expressions $r_1(t) = r_0 + \tilde{r}_1(t)\mathcal{H}(t)$, $\theta_1(t) = \omega t + \tilde{\theta}_1(t)\mathcal{H}(t)$, $r_2(t) = r_0 + \tilde{r}_2(t)\mathcal{H}(t)$, and $\theta_2(t) = \omega t + \pi + \tilde{\theta}_2(t)\mathcal{H}(t)$ into (3), $\mathcal{H}$ being the Heaviside function. Taking the Laplace transform of the linearized equations (A2), we obtain algebraic equations for the Laplace transformed variables $R_i(s) = \mathcal{L}[\tilde{r}_i(s)]$ and $\Theta_i(s) = \mathcal{L}[\tilde{\theta}_i(s)]$, which may be expressed in matrix form as

$$\begin{pmatrix} A(s) & -B(s) & -E(s) & -F(s) \\ C(s) & D(s) & G(s) & H(s) \\ -E(s) & -F(s) & A(s) & -B(s) \\ G(s) & H(s) & C(s) & D(s) \end{pmatrix} \begin{pmatrix} R_1 \\ r_0\Theta_1 \\ R_2 \\ r_0\Theta_2 \end{pmatrix} = \begin{pmatrix} c_{r_1} \\ r_0 c_{\theta_1} \\ c_{r_2} \\ r_0 c_{\theta_2} \end{pmatrix}. \tag{8}$$

The matrix elements of the 4×4 matrix are defined through the functions given in Eq. (A3) in the Appendix. The constants on the right-hand side of this equation are defined through the initial conditions by $\dot{\tilde{r}}_i(0) = c_{r_i}/\kappa$ and $\dot{\tilde{\theta}}_i(0) = c_{\theta_i}/\kappa$, where we assume that $\tilde{r}_i(0) = \tilde{\theta}_i(0) = 0$ [19].

The eigenvalues of the linear stability problem are given by the poles of the Laplace transforms $R_i(s)$ and $\Theta_i(s)$ [19]. The orbital solution is stable if all eigenvalues satisfy $\mathrm{Re}(s) < 0$, and unstable otherwise. The function $f(r,t)$ decays exponentially in t, $f \sim \mathrm{e}^{-t}$ as $t \to \infty$, which implies that the functions in (A3) are analytic in the region $\mathrm{Re}(s) \geqslant 0$. The unstable eigenvalues of the linear stability problem are thus given by the zeros of $\det \mathbf{M}(s)$, where $\mathbf{M}(s)$ is the 4×4 matrix in (8). For square matrices M_1 and M_2, we have the identity

$$\det \begin{pmatrix} M_1 & M_2 \\ M_2 & M_1 \end{pmatrix} = \det(M_1 - M_2) \cdot \det(M_1 + M_2), \tag{9}$$

from which we deduce that $\det \mathbf{M}(s) = \mathcal{G}_+(s)\mathcal{G}_-(s)$, where

$$\mathcal{G}_\pm(s) = [A(s) \pm E(s)][D(s) \mp H(s)] + [B(s) \mp F(s)][C(s) \mp G(s)]. \tag{10}$$

The linear stability problem is thus reduced to finding the roots of $\mathcal{G}_{\pm}(s)$ in the right-half complex plane. It may be shown that $\mathcal{G}_{+}(\pm i\omega) = 0$ and $\mathcal{G}_{-}(0) = 0$, which reflect the invariance of the orbital solution under translation and rotation, respectively [19]. To locate the nontrivial roots of $\mathcal{G}_{\pm}(s)$, we use the contour integration method developed by Delves and Lyness [43]. A circular orbit is stable if there are no roots in the region $\mathrm{Re}(s) > 0$ (blue curves in Fig. 8), and unstable otherwise. For unstable orbits, we identify the root s^* of $\det \mathbf{M}(s)$ with the largest real part. Orbits with $\mathrm{Im}(s^*) = 0$ destabilize via a non-oscillatory instability (red curves in Fig. 8), and those with $\mathrm{Im}(s^*) \neq 0$ destabilize via an oscillatory instability (green curves).

We find that unstable (red) branches separate the quantized circular and wobbling orbital solutions, which was also observed in theoretical studies of a single walker in a rotating frame [19] and harmonic potential [20]. However, we find that circular orbits undergo oscillatory instabilities at low and high memories [Fig. 8(c)] and are stabilized at intermediate memories for $n \leqslant 2$, which is consistent with experiment (Fig. 4). This is in contrast to a single walker's dynamics in the presence of external forces, in which orbits are stable at low memory and destabilize as the memory is progressively increased [18–21].

To understand the effects of nonlinearity in the unstable regimes, we performed numerical simulations of the trajectory equation (3) with adaptive phase, using a fourth-order Adams-Bashforth time-stepping method combined with Simpson's integration rule [44]. Some unstable circular orbits destabilize into wobbling orbits, the extent of the wobbling being indicated by the shaded green regions in Fig. 8, while others destabilize into rectilinear walking states. For the parameter values explored here, we find that a necessary (but not sufficient) condition for a stable wobbling orbit is that the unstable eigenvalues of the linear stability problem consist of a single complex-conjugate pair that are roots of $\mathcal{G}_{-}(s)$; indeed, wobbling orbits are never found near the red solution branches in Fig. 8, which destabilize via non-oscillatory instabilities. Examples of simulated wobbling orbits are shown in Fig. 10, both at low memory (panels a and b) and high memory (panel c). We observe various polygonal instabilities of orbital solutions at low memory [Figs. 10(a)–10(b)], qualitatively similar to the high-frequency wobbling orbits observed in experiments [Fig. 4(a)]. Both 2ω- and 3ω-wobbling orbits are observed at high memory [Fig. 10(c)], as in the experiments [Figs. 4(b)–4(c)]. The wobbling amplitudes [Fig. 8(c)] exhibit the qualitative behavior characteristic of supercritical Hopf bifurcations, as observed experimentally [Fig. 5(a)]. We also observe presumably chaotic trajectories, in which the separation distance between the walkers $d(t)$ is aperiodic.

Figure 8(c) shows that we obtain stable orbits, wobbling orbits, and unstable orbits in a wide range of both orbit order ($n \geqslant 1$) and memory, as observed in the experiments. It is evident that phase adaptation through the phase parameter $\mathcal{S} = \mathcal{S}(h)$ has a stabilizing effect on both circular and wobbling orbits, thus substantially improving the match with experiment. Specifically, the theoretical model that assumes constant phase [Fig. 8(b)] incorrectly predicts the absence of bound states for $n = 3$ and $n = 3.5$, a failing that is corrected by the inclusion of phase adaptation [Fig. 8(c)]. Comparison of Figs. 8(b) and 8(c) also indicates that wobbling orbits are observed over a larger range of forcing acceleration γ/γ_F for each orbit order n in the model that includes phase adaptation.

While including the dependence of the phase parameter on forcing acceleration and local wave height improves the comparison with experiments, the match in Fig. 8(c) is still imperfect. First, we obtain no solutions for the smallest orbit $n = 0.5$, which is presumably due to the model's poor characterization of the waves in the near-field. The model for the wave field (2) is derived under the assumption that the walker is a point source [30], an approximation that is evidently inadequate when the orbital radius is comparable to the drop radius. Second, the orbits predicted by our stroboscopic model become unbound at high memory ($\gamma/\gamma_F > 0.92$), unlike in the experiments. This discrepancy might be explained by the fact that more complicated bouncing states, which are not adequately described by the stroboscopic model, may arise at high memory. Specifically, as indicated in Fig. 1(d), the experimental results of Wind-Willassen *et al.* [45] indicate that our drops of vibration number $2\pi f_0/\sqrt{\sigma/\rho R^3} \approx 0.77$ would transition to a (4,2) bouncing state at $\gamma/\gamma_F \approx 0.93$, and to a chaotic bouncing state at $\gamma/\gamma_F \approx 0.97$.

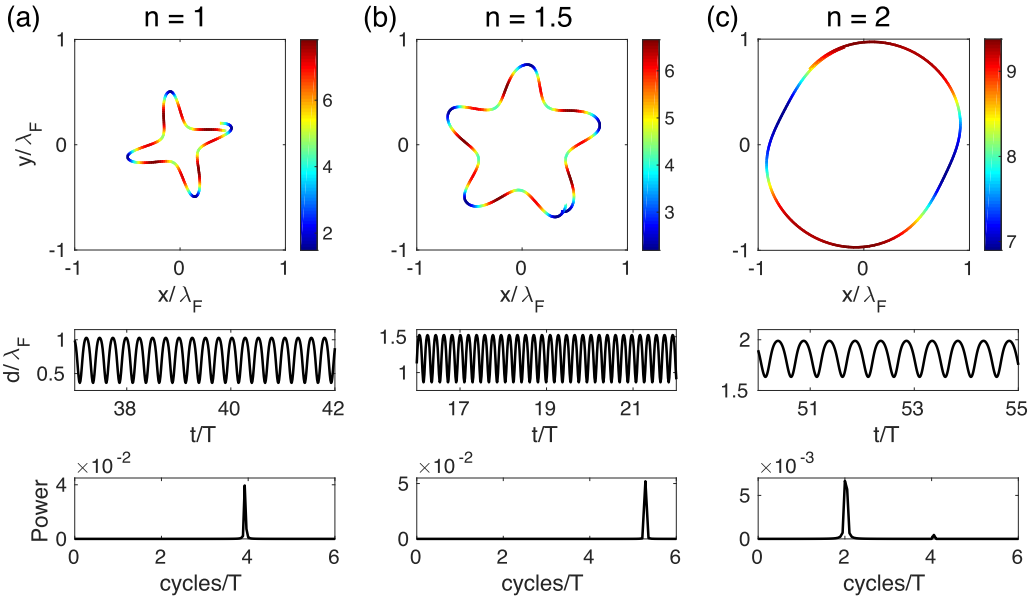

FIG. 10. Simulations of the trajectory equation (3) in three different parameter regimes, showing the emergence of wobbling orbits. The first row shows the trajectory of a walker color-coded according to its speed (mm/s), the other walker (not shown) being diametrically opposed. The second row shows the time evolution of the distance $d(t) = |\boldsymbol{x}_1(t) - \boldsymbol{x}_2(t)|$ between the walkers, T being the orbital period. The third row shows the power spectrum of the distance $d(t)$, which confirms that the solutions are roughly (a) 4ω-, (b) 5ω-, and (c) 2ω-wobbling orbits. The forcing accelerations are (a) $\gamma/\gamma_F = 0.784$, (b) $\gamma/\gamma_F = 0.776$, and (c) $\gamma/\gamma_F = 0.888$.

IV. CONCLUSION

We have examined the dynamics of orbiting pairs of walkers of equal size, focusing on the influence of memory on the stability of the quantized orbits. Small orbits are stable for large values of forcing acceleration but wobble in the low-memory limit. Conversely, large orbits ($n > 2$) destabilize at high memory, the stable region of parameter space shrinking with orbital diameter. The precision of our experimental setup allowed us to observe the $n = 3$ and $n = 3.5$ orbits, which were not reported in prior experiments [22,28]. The speeds of the orbiting drops increase with orbital diameter and may exceed the free walking speed of a single walker for large wobbling orbits. We also observed a 3ω-wobbling solution, an orbital bound state in which the separation distance between the walkers oscillates at roughly thrice the orbital frequency. Our experiments have guided the refinement of our theoretical models of pilot-wave hydrodynamics.

We extended the stroboscopic model [31] to capture theoretically the walker-walker interactions and the transition from stable to wobbling orbits. Specifically, the model was extended to include spatial damping of the wave field, the importance of which was indicated by recent experimental measurements [42], and allows for the phase of impact to vary with the forcing acceleration and local wave height. The extended model predicts the orbital diameters well [Fig. 8(c)] and qualitatively reproduces the emergence of wobbling orbits (Fig. 10). We identify the walkers' phase adaptation to the local wave height as the cause for their decreased speeds in tighter orbits [Fig. 9(b)]. Phase adaptation is also shown to have a stabilizing effect on both circular and wobbling orbits [Figs. 8(b)–8(c)]. The shortcomings of the model have also been identified and rationalized. Specifically, the stroboscopic model fails to capture the smallest $n = 0.5$ orbits because the wave field near the drop impact is inadequately described. The model predictions also break down at high memory, when the walker ceases to execute a $(2,1)$ bouncing mode and instead enters a $(4,2)$ mode or chaotic walking state [45].

The functional dependence of the phase $\mathcal{S} = \sin\Phi$ on forcing acceleration and wave height cannot be deduced from the stroboscopic model (3), as it does not include the walker's vertical dynamics, so we instead inferred a semiempirical linear dependence in Sec. III B. Alternatively, we may use Moláček and Bush's model of the walker's coupled horizontal and vertical dynamics [4,30]. As their model has no free parameters, the phase parameter $\mathcal{S}$ is computed directly from the simulated solution. This approach will provide a theoretical prediction for the phase dependence $\mathcal{S}(\gamma/\gamma_F,h)$, roughly consistent with that inferred here, that can be incorporated into our adaptive-phase stroboscopic model, a direction to be explored in a forthcoming publication [40].

Our analysis of orbiting pairs suggests that a walker behaves as a phase-adapting oscillator, maintaining a periodic bouncing dynamics by modifying its impact phase according to the local wave height. The idea of phase adaptation explains why interacting walkers move slower than free ones, suggesting an effective binding energy between walkers [29]. It also may provide theoretical insight into lattices [46,47], ratcheting pairs [48], promenade modes [29], and other complex bound states reported in recent experiments. Rationalizing the dependence of phase on wave height and incorporating it into the stroboscopic model will be the subject of future work [40].

ACKNOWLEDGMENTS

The authors gratefully acknowledge Ruben Rosales, Giuseppe Pucci, Pedro Sáenz, and Juncal Arbelaiz for valuable conversations and assistance. J.B. gratefully acknowledges the financial support of the NSF through grants CMMI-1333242 and DMS-1614043, the MIT-Brazil Program and the CNPq-Science Without Borders Program. A.O. acknowledges the support of the NSF Mathematical Sciences Postdoctoral Research Fellowship.

APPENDIX

The trajectory equation in polar coordinates is

$$\begin{aligned}\kappa\left(\ddot{r}_1 - r_1\dot{\theta}_1^2\right) + \dot{r}_1 = &-\beta\mathcal{S}(h_1(\boldsymbol{x}_1(t),t))\int_{-\infty}^{t}\left\{\frac{f_r(|\boldsymbol{x}_1(t)-\boldsymbol{x}_1(s)|,t-s)}{|\boldsymbol{x}_1(t)-\boldsymbol{x}_1(s)|}(r_1(t)-r_1(s)\cos[\theta_1(t)\right.\\ &\left.-\theta_1(s)]) + \varsigma\frac{f_r(|\boldsymbol{x}_1(t)-\boldsymbol{x}_2(s)|,t-s)}{|\boldsymbol{x}_1(t)-\boldsymbol{x}_2(s)|}(r_1(t)-r_2(s)\cos[\theta_1(t)-\theta_2(s)])\right\}ds,\\ \kappa(2\dot{r}_1\dot{\theta}_1 + r_1\ddot{\theta}_1) + r_1\dot{\theta}_1 = &-\beta\mathcal{S}(h_1(\boldsymbol{x}_1(t),t))\int_{-\infty}^{t}\left\{\frac{f_r(|\boldsymbol{x}_1(t)-\boldsymbol{x}_1(s)|,t-s)}{|\boldsymbol{x}_1(t)-\boldsymbol{x}_1(s)|}r_1(s)\sin[\theta_1(t)-\theta_1(s)]\right.\\ &\left.+\varsigma\frac{f_r(|\boldsymbol{x}_1(t)-\boldsymbol{x}_2(s)|,t-s)}{|\boldsymbol{x}_1(t)-\boldsymbol{x}_2(s)|}r_2(s)\sin[\theta_1(t)-\theta_2(s)]\right\}ds, \qquad \text{(A1)}\end{aligned}$$

where h_1 is defined in (3). The equation for $\boldsymbol{x}_2(t)$ is obtained simply by interchanging $1 \leftrightarrow 2$ in (A1). We substitute the expressions $r_1(t) = r_0 + \tilde{r}_1(t)\mathcal{H}(t)$, $\theta_1(t) = \omega t + \tilde{\theta}(t)\mathcal{H}(t)$, $r_2(t) = r_0 + \tilde{r}_2(t)\mathcal{H}(t)$, and $\theta_2(t) = \omega t + \pi + \tilde{\theta}_2(t)\mathcal{H}(t)$ into (A1) and retain terms at leading order in the perturbations $\tilde{r}_i(t),\tilde{\theta}_i(t)$, where r_0,ω are defined by (4) and $\mathcal{H}$ is the Heaviside function. We thus obtain the linearized equations (dropping all tildes)

$$\begin{aligned}&\kappa(\ddot{r}_1 - \omega^2 r_1 - 2r_0\omega\dot{\theta}_1) + \dot{r}_1\\ &= \beta\mathcal{S}\int_{-\infty}^{t}\left(\hat{S}(z)\cos\frac{\omega z}{2}\left\{[r_1(t)-r_1(s)\mathcal{H}(s)]\cos\frac{\omega z}{2} + r_0[\theta_1(t)-\theta_1(s)\mathcal{H}(s)]\sin\frac{\omega z}{2}\right\}\right.\\ &\quad + \hat{S}_2(z)\sin\frac{\omega z}{2}\left\{[r_1(t)+r_1(s)\mathcal{H}(s)]\sin\frac{\omega z}{2} + r_0[\theta_1(t)-\theta_1(s)\mathcal{H}(s)]\cos\frac{\omega z}{2}\right\}\\ &\quad \left.+\varsigma\hat{C}(z)\sin\frac{\omega z}{2}\left\{[r_1(t)-r_2(s)\mathcal{H}(s)]\sin\frac{\omega z}{2} - r_0[\theta_1(t)-\theta_2(s)\mathcal{H}(s)]\cos\frac{\omega z}{2}\right\}\right.\end{aligned}$$

$$+\varsigma C_2(z)\cos\frac{\omega z}{2}\Big\{[r_1(t)+r_2(s)\mathcal{H}(s)]\cos\frac{\omega z}{2}-r_0[\theta_1(t)-\theta_2(s)\mathcal{H}(s)]\sin\frac{\omega z}{2}\Big\}\Big)\,ds$$
$$+\frac{\kappa r_0\omega^2\mathcal{S}'}{\mathcal{S}}\int_{-\infty}^{t}\Big(S_1(z)\Big\{(r_1(t)+r_1(s)\mathcal{H}(s))\sin\frac{\omega z}{2}+r_0\cos\frac{\omega z}{2}(\theta_1(t)-\theta_1(s)\mathcal{H}(s))\Big\}$$
$$+\varsigma C_1(z)\Big\{[r_1(t)+r_2(s)\mathcal{H}(s)]\cos\frac{\omega z}{2}-r_0\sin\frac{\omega z}{2}[\theta_1(t)-\theta_2(s)\mathcal{H}(s)]\Big\}\Big)\,ds,$$

$$\kappa(2\omega\dot{r}_1+r_0\ddot{\theta}_1)+\omega r_1+r_0\dot{\theta}_1$$
$$=\beta\mathcal{S}\int_{-\infty}^{t}\Big(\hat{S}(z)\Big\{-\frac{1}{2}[r_1(t)-r_1(s)\mathcal{H}(s)]\sin\omega z-r_0[\theta_1(t)-\theta_1(s)\mathcal{H}(s)]\sin^2\frac{\omega z}{2}\Big\}$$
$$+S_2(z)\Big\{\frac{1}{2}[r_1(t)+r_1(s)\mathcal{H}(s)]\sin\omega z+r_0\cos^2\frac{\omega z}{2}[\theta_1(t)-\theta_1(s)\mathcal{H}(s)]\Big\}$$
$$+\varsigma\hat{C}(z)\Big\{\frac{1}{2}[r_1(t)-r_2(s)\mathcal{H}(s)]\sin\omega z-r_0[\theta_1(t)-\theta_2(s)\mathcal{H}(s)]\cos^2\frac{\omega z}{2}\Big\}$$
$$+\varsigma C_2(z)\Big\{-\frac{1}{2}[r_1(t)+r_2(s)\mathcal{H}(s)]\sin\omega z+r_0\sin^2\frac{\omega z}{2}[\theta_1(t)-\theta_2(s)\mathcal{H}(s)]\Big\}\Big)\,ds$$
$$-\frac{r_0\omega\mathcal{S}'}{\mathcal{S}}\int_{-\infty}^{t}\Big(S_1(z)\Big\{[r_1(t)+r_1(s)\mathcal{H}(s)]\sin\frac{\omega z}{2}+r_0\cos\frac{\omega z}{2}[\theta_1(t)-\theta_1(s)\mathcal{H}(s)]\Big\}$$
$$+\varsigma C_1(z)\Big\{[r_1(t)+r_2(s)\mathcal{H}(s)]\cos\frac{\omega z}{2}-r_0\sin\frac{\omega z}{2}[\theta_1(t)-\theta_2(s)\mathcal{H}(s)]\Big\}\Big)\,ds, \tag{A2}$$

where $z=t-s$, $\hat{S}(z)=S_1(z)/2r_0\sin(\omega z/2)$, $\hat{C}(z)=C_1(z)/2r_0\cos(\omega z/2)$, and $\mathcal{S}=\mathcal{S}(h_c),\mathcal{S}'=\mathcal{S}'(h_c)=p_3$ are evaluated at the wave field h_c as defined in Eq. (6). We obtain analogous equations for the perturbations $r_2(t)$ and $\theta_2(t)$ to the other walker's trajectory.

The functions defined in the main text are obtained by taking the Laplace transform of both sides of (A2) and are given by

$$A(s)=\kappa s^2+s-\kappa\omega^2-\varsigma\beta\mathcal{I}\Big[\hat{C}(z)\sin^2\frac{\omega z}{2}+C_2(z)\cos^2\frac{\omega z}{2}\Big]+\beta\mathcal{L}_-\Big[\hat{S}(z)\cos^2\frac{\omega z}{2}\Big]$$
$$-\beta\mathcal{L}_+\Big[S_2(z)\sin^2\frac{\omega z}{2}\Big]-\frac{\kappa r_0\omega^2\mathcal{S}'}{\mathcal{S}}\Big\{\mathcal{I}\Big[S_1(z)\sin\frac{\omega z}{2}+\varsigma C_1(z)\cos\frac{\omega z}{2}\Big]+\mathcal{L}\Big[S_1(z)\sin\frac{\omega z}{2}\Big]\Big\},$$

$$B(s)=2\kappa\omega s-\frac{\varsigma\beta}{2}\mathcal{I}\{[\hat{C}(z)+C_2(z)]\sin\omega z\}-\frac{\beta}{2}\mathcal{L}_-\{[\hat{S}(z)+S_2(z)]\sin\omega z\}$$
$$-\frac{\kappa r_0\omega^2\mathcal{S}'}{\mathcal{S}}\Big\{\mathcal{I}\Big[-S_1(z)\cos\frac{\omega z}{2}+\varsigma C_1(z)\sin\frac{\omega z}{2}\Big]+\mathcal{L}\Big[S_1(z)\cos\frac{\omega z}{2}\Big]\Big\},$$

$$C(s)=2\omega\kappa s+\omega-\frac{\varsigma\beta}{2}\mathcal{I}[(\hat{C}(z)-C_2(z))\sin\omega z]-\frac{\beta}{2}\mathcal{L}_-[\hat{S}(z)\sin\omega z]-\frac{\beta}{2}\mathcal{L}_+[S_2(z)\sin\omega z]$$
$$+\frac{r_0\omega\mathcal{S}'}{\mathcal{S}}\Big\{\mathcal{I}\Big[S_1(z)\sin\frac{\omega z}{2}+\varsigma C_1(z)\cos\frac{\omega z}{2}\Big]+\mathcal{L}\Big[S_1(z)\sin\frac{\omega z}{2}\Big]\Big\},$$

$$D(s)=\kappa s^2+s-\varsigma\beta\mathcal{I}\Big[-\hat{C}(z)\cos^2\frac{\omega z}{2}+C_2(z)\sin^2\frac{\omega z}{2}\Big]+\beta\mathcal{L}_-\Big[S_2(z)\cos^2\frac{\omega z}{2}-\hat{S}(z)\sin^2\frac{\omega z}{2}\Big]$$
$$-\frac{r_0\omega\mathcal{S}'}{\mathcal{S}}\Big\{\mathcal{I}\Big[-S_1(z)\cos\frac{\omega z}{2}+\varsigma C_1(z)\sin\frac{\omega z}{2}\Big]+\mathcal{L}\Big[S_1(z)\cos\frac{\omega z}{2}\Big]\Big\},$$

$$E(s) = \varsigma\beta\mathcal{L}\Big[-\hat{C}(z)\sin^2\frac{\omega z}{2} + C_2(z)\cos^2\frac{\omega z}{2}\Big] + \frac{\varsigma\kappa r_0\omega^2\mathcal{S}'}{\mathcal{S}}\mathcal{L}\Big[C_1(z)\cos\frac{\omega z}{2}\Big],$$

$$F(s) = \frac{\varsigma\beta}{2}\mathcal{L}[(\hat{C}(z) + C_2(z))\sin\omega z] + \frac{\varsigma\kappa r_0\omega^2\mathcal{S}'}{\mathcal{S}}\mathcal{L}\Big[C_1(z)\sin\frac{\omega z}{2}\Big],$$

$$G(s) = \frac{\varsigma\beta}{2}\mathcal{L}[(\hat{C}(z) + C_2(z))\sin\omega z] + \frac{\varsigma r_0\omega\mathcal{S}'}{\mathcal{S}}\mathcal{L}\Big[C_1(z)\cos\frac{\omega z}{2}\Big],$$

$$H(s) = -\varsigma\beta\mathcal{L}\Big[\hat{C}(z)\cos^2\frac{\omega z}{2} - C_2(z)\sin^2\frac{\omega z}{2}\Big] + \frac{\varsigma r_0\omega\mathcal{S}'}{\mathcal{S}}\mathcal{L}\Big[C_1(z)\sin\frac{\omega z}{2}\Big], \tag{A3}$$

where we define $\mathcal{L}[g(t)] = \int_0^\infty g(t)\mathrm{e}^{-st}\,dt$, $\mathcal{L}_\pm[g(t)] = \int_0^\infty g(t)(\mathrm{e}^{-st} \pm 1)\,dt$, and $\mathcal{I}[g(t)] = \int_0^\infty g(t)\,dt$.

[1] Y. Couder, S. Protière, E. Fort, and A. Boudaoud, Walking and orbiting droplets, Nature (London) **437**, 208 (2005).

[2] Y. Couder, E. Fort, C.-H. Gautier, and A. Boudaoud, From Bouncing to Floating: Non-Coalescence of Drops on a Fluid Bath, Phys. Rev. Lett. **94**, 177801 (2005).

[3] S. Dorbolo, D. Terwagne, N. Vandewalle, and T. Gilet, Resonant and rolling droplet, New J. Phys. **10**, 113021 (2008).

[4] J. Moláček and J. W. M. Bush, Drops bouncing on a vibrating bath, J. Fluid Mech. **727**, 582 (2013).

[5] D. Terwagne, N. Vandewalle, and S. Dorbolo, Lifetime of a bouncing droplet, Phys. Rev. E **76**, 056311 (2007).

[6] F. Blanchette, Modeling the vertical motion of drops bouncing on a bounded fluid reservoir, Phys. Fluids **28**, 032104 (2016).

[7] T. Gilet, D. Terwagne, N. Vandewalle, and S. Dorbolo, Dynamics of a Bouncing Droplet Onto a Vertically Vibrated Interface, Phys. Rev. Lett. **100**, 167802 (2008).

[8] M. Hubert, F. Ludewig, S. Dorbolo, and N. Vandewalle, Bouncing dynamics of a spring, Physica D **272**, 1 (2014).

[9] S. Protière, A. Boudaoud, and Y. Couder, Particle-wave association on a fluid interface, J. Fluid. Mech. **554**, 85 (2006).

[10] T. B. Benjamin and F. Ursell, The stability of the plane free surface of a liquid in vertical periodic motion, Proc. R. Soc. Lond. A **225**, 505 (1954).

[11] K. Kumar and L. S. Tuckerman, Parametric instability of the interface between two fluids, J. Fluid Mech. **279**, 49 (1994).

[12] A. Eddi, E. Sultan, J. Moukhtar, E. Fort, M. Rossi, and Y. Couder, Information stored in Faraday waves: The origin of a path memory, J. Fluid Mech. **674**, 433 (2011).

[13] A. Andersen, J. Madsen, C. Reichelt, S. R. Ahl, B. Lautrup, C. Ellegaard, M. T. Levinsen, and T. Bohr, Double-slit experiment with single wave-driven particles and its relation to quantum mechanics, Phys. Rev. E **92**, 013006 (2015).

[14] Y. Couder and E. Fort, Single-Particle Diffraction and Interference at a Macroscopic Scale, Phys. Rev. Lett. **97**, 154101 (2006).

[15] T. Gilet, Dynamics and statistics of wave-particle interactions in a confined geometry, Phys. Rev. E **90**, 052917 (2014).

[16] D. M. Harris, J. Moukhtar, E. Fort, Y. Couder, and J. W. M. Bush, Wavelike statistics from pilot-wave dynamics in a circular corral, Phys. Rev. E **88**, 011001(R) (2013).

[17] A. Eddi, E. Fort, F. Moisy, and Y. Couder, Unpredictable Tunneling of a Classical Wave-Particle Association, Phys. Rev. Lett. **102**, 240401 (2009).

[18] D. M. Harris and J. W. M. Bush, Droplets walking in a rotating frame: From quantized orbits to multimodal statistics, J. Fluid Mech. **739**, 444 (2014).
[19] A. U. Oza, D. M. Harris, R. R. Rosales, and J. W. M. Bush, Pilot-wave dynamics in a rotating frame: On the emergence of orbital quantization, J. Fluid Mech. **744**, 404 (2014).
[20] M. Labousse, A. U. Oza, S. Perrard, and J. W. M. Bush, Pilot-wave dynamics in a harmonic potential: Quantization and stability of circular orbits, Phys. Rev. E **93**, 033122 (2016).
[21] S. Perrard, M. Labousse, M. Miskin, E. Fort, and Y. Couder, Self-organization into quantized eigenstates of a classical wave-driven particle, Nat. Commun. **5**, 3219 (2014).
[22] A. Eddi, J. Moukhtar, S. Perrard, E. Fort, and Y. Couder, Level Splitting at Macroscopic Scale, Phys. Rev. Lett. **108**, 264503 (2012).
[23] J. W. M. Bush, Pilot-wave hydrodynamics, Ann. Rev. Fluid Mech. **47**, 269 (2015).
[24] M. Labousse, Étude d'une dynamique à mémoire de chemin: une expérimentation théorique, Ph.D. thesis, Université Pierre et Marie Curie UPMC Paris VI (2014).
[25] L. de Broglie, *Ondes et mouvements* (Gauthier-Villars, Paris, 1926).
[26] J. W. M. Bush, The new wave of pilot-wave theory, Phys. Today **68**, 47 (2015).
[27] S. Protière, Gouttes rebondissantes: Une association onde-particule à échelle macroscopique, Ph.D. thesis, Université Paris Diderot (2007).
[28] S. Protière, S. Bohn, and Y. Couder, Exotic orbits of two interacting wave sources, Phys. Rev. E **78**, 036204 (2008).
[29] C. Borghesi, J. Moukhtar, M. Labousse, A. Eddi, E. Fort, and Y. Couder, Interaction of two walkers: Wave-mediated energy and force, Phys. Rev. E **90**, 063017 (2014).
[30] J. Moláček and J. W. M. Bush, Drops walking on a vibrating bath: Towards a hydrodynamic pilot-wave theory, J. Fluid Mech. **727**, 612 (2013).
[31] A. U. Oza, R. R. Rosales, and J. W. M. Bush, A trajectory equation for walking droplets: Hydrodynamic pilot-wave theory, J. Fluid Mech. **737**, 552 (2013).
[32] P. A. Milewski, C. A. Galeano-Rios, A. Nachbin, and J. W. M. Bush, Faraday pilot-wave dynamics: Modelling and computation, J. Fluid Mech. **778**, 361 (2015).
[33] R. Dubertrand, M. Hubert, P. Schlagheck, N. Vandewalle, T. Bastin, and J. Martin, Scattering theory of walking droplets in the presence of obstacles, New J. Phys. **18**, 113037 (2016).
[34] M. Durey and P. A. Milewski, Faraday wave-droplet dynamics: Discrete-time analysis, J. Fluid Mech. (unpublished).
[35] L. M. Faria, A model for Faraday pilot-waves over variable topography, J. Fluid Mech. **811**, 51 (2017).
[36] D. M. Harris and J. W. M. Bush, Generating uniaxial vibration with an electrodynamic shaker and external air bearing, J. Sound Vib. **334**, 255 (2015).
[37] D. M. Harris, T. Liu, and J. W. M. Bush, A low-cost, precise piezoelectric droplet-on-demand generator, Exp. Fluids **56**, 83 (2015).
[38] G. Pucci, P. J. Sáenz, L. M. Faria, and J. W. M. Bush, Non-specular reflection of walking droplets, J. Fluid Mech. **804**, R3 (2016).
[39] See Supplemental Material at http://link.aps.org/supplemental/10.1103/PhysRevFluids.2.053601 for a video of a pair of walkers orbiting in phase in the $n = 1$ orbital mode.
[40] J. Moláček, A. U. Oza, S. Turton, and J. W. M. Bush, Refinements in the theoretical modeling of walking droplets (unpublished).
[41] E. Fort, A. Eddi, A. Boudaoud, J. Moukhtar, and Y. Couder, Path-memory induced quantization of classical orbits, Proc. Natl. Acad. Sci. USA **107**, 17515 (2010).
[42] A. P. Damiano, P.-T Brun, D. M. Harris, C. A. Galeano-Rios, and J. W. M. Bush, Surface topography measurements of the bouncing droplet experiment, Exp. Fluids **57**, 163 (2016).
[43] L. M. Delves and J. N. Lyness, A numerical method for locating the zeros of an analytic function, Math. Comput. **21**, 543 (1967).
[44] A. U. Oza, Ø. Wind-Willassen, D. M. Harris, R. R. Rosales, and J. W. M. Bush, Pilot-wave hydrodynamics in a rotating frame: Exotic orbits, Phys. Fluids **26**, 082101 (2014).
[45] Ø. Wind-Willasen, J. Moláček, D. M. Harris, and J. W. M. Bush, Exotic states of bouncing and walking droplets, Phys. Fluids **25**, 082002 (2013).

[46] A. Eddi, A. Boudaoud, and Y. Couder, Oscillating instability in bouncing droplet crystals, Europhys. Lett. **94**, 20004 (2011).

[47] A. Eddi, A. Decelle, E. Fort, and Y. Couder, Archimedean lattices in the bound states of wave interacting particles, Europhys. Lett. **87**, 56002 (2009).

[48] A. Eddi, D. Terwagne, E. Fort, and Y. Couder, Wave propelled ratchets and drifting rafts, Europhys. Lett. **82**, 44001 (2008).